# Long-time semiclassical dynamics of chaos: The stadium billiard

Steven Tomsovic and Eric J. Heller

*Department of Physics and Department of Chemistry, BG-10, University of Washington, Seattle, Washington 98195*
(Received 6 July 1992)

In a recent Letter [Phys. Rev. Lett. **67**, 664 (1991)] we found semiclassical propagation to be remarkably accurate in the chaotic stadium billiard long after classical fine structure had developed on a scale much smaller than $\hbar$. We give a complete account of that work and derive an approximate time scale for the validity of the semiclassical approximation as a function of $\hbar$.

PACS number(s): 05.45.+b, 03.65.Sq, 03.40.Kf

## I. INTRODUCTION

Since its inception in the form of the "old quantum theory," semiclassical mechanics has been an essential component in the understanding of a variety of physical systems, providing a bridge between the quantum and classical worlds. A rigorous mathematical framework for semiclassical methods was constructed by Maslov and Fedoriuk [1]. The eigenvalue spectrum according to semiclassical approximation was embodied in the trace formula of Gutzwiller [2] (see also Balian and Bloch [3]). In spite of these advances, crucial questions were left unanswered. There is now a renaissance in the development and applications of semiclassical techniques [4–7]. It is in good measure driven by some long-standing questions about the fundamental nature of the correspondence principle (see Jensen, Ref. [8]). A common thread amongst many of the most interesting outstanding problems concerns the difficulties, both theoretical and practical, introduced by the presence of chaotic motion in the dynamics of a quantum system's classical analog.

The major thrust of research into the semiclassical mechanics of chaos has been in periodic orbit theory [2, 5]. Gutzwiller's derivation of the trace formula served as a catalyst for this growing subject. Periodic orbit theory generates quantum eigenvalue information simply from the characteristics of the classical periodic orbits. Attempts to reproduce detailed spectra in the chaotic regime have proven difficult, but the introduction of new summation techniques has given much cause for optimism [5]. Some efforts along these lines to infer eigenstate properties also exist [9, 10]. Unfortunately, justification of the semiclassical trace formula is still an open problem [11] and it is unclear whether the troublesome periodic orbit sum converges to the quantum spectrum in any sensible way.

There is an alternative time domain, dynamical approach based on the semiclassical Van Vleck–Gutzwiller (VVG) Green's-function propagator [12, 13]. By pursuing the dynamical approach, we have two goals. The first is the development of practical semiclassical techniques, workable even if the dynamics are complicated. They would be of direct interest applied to studies of time-dependent phenomena in atomic, molecular, wave guide, and other systems. Second, we get new insight into semiclassical aspects of chaos and the correspondence principle issues mentioned above. The fact that the VVG propagator plays a crucial role in the derivation of the trace formula also means that its validity has direct, important consequences in periodic orbit theory. The successes of periodic orbit theory should ultimately be linked to the validity of the dynamical approximation.

In the very-short-time regime there is no substantive difference between integrable and chaotic motion and semiclassical mechanics works equally well for both kinds of motion, as it must. Beyond this regime, integrable and chaotic motion reveal themselves to be distinct at ever finer scales in phase space. In the integrable case, the motion is quasiperiodic and the local dynamics increases complexity linearly in time. In contrast, the chaotic evolution appears to be almost random and it develops fine phase-space structure exponentially fast. The question becomes: what kinds of evolving structures (and on what scale) can semiclassical mechanics reliably use to approximate quantum dynamics accurately?

For these reasons, we have been developing techniques to study long-time semiclassical dynamics. We found some rather encouraging results beginning with an integrable system, the Morse oscillator [14]. Then, in two parallel studies of chaotic systems, one on the baker's map [15] and one on the stadium billiard [4], the long-time semiclassical dynamics again proved to be extraordinarily accurate. More recently, our work has been extended to the more "generic" kicked rotor. This work is helping to clear up some of the mysteries surrounding the unexpectedly accurate approximations [16].

Surprisingly, very little work along these lines had been published before, with the notable exceptions mentioned just ahead. The semiclassical propagator had not previously been systematically tested for a system far from integrability. This may have been due to technical barriers to assembling the necessary semiclassical information, or perhaps to pessimism about the applicability of semiclassical dynamics to chaotic systems. Loosely, the gloomy picture was as follows. The nonzero size of Planck's constant must be responsible for some kind of smoothing over the intricate complexity that is the essence of chaotic dynamics (or the intricate coexistence of regu-

lar and chaotic motion found in mixed systems), so why bother investigating the effects of classical structures on a scale far finer than a Planck cell? This is a logical trap. Although the nonzero size of $\hbar$ implies that quantum mechanics cannot be used to retrieve the detailed classical motion, it does not necessarily follow that the classical details cannot underlie or be used to predict the quantum mechanics—that question is our central concern here.

The prior theoretical treatment addressing the time-interval versus dynamics question is mainly that of Berry and Balazs [17] and Berry et al. [18, 19]. They described a formidable time-scale barrier which semiclassical mechanics seemed unable to penetrate. They argued that the semiclassical evolution of a state under chaotic dynamics remains accurate only over an extremely short time $t^* = O(\ln(\hbar^{-1}))$, which is dubbed the "log time." Roughly speaking, beyond $t^*$ the usual stationary-phase approximation, which is the foundation stone of semiclassical mechanics, should collapse. At issue is whether the stationary-phase points (classical orbits) are sufficiently well isolated. In a bounded chaotic system, they apparently begin coalescing in great numbers on the scale of $t^*$, leading to the expectation that the semiclassical approximation should be headed for a total collapse by that time. The logarithmic dependence is an expression of the exponential instability of neighboring classical trajectories. In this light, the findings of our recent studies led to quite unexpected results. The evidence in the baker's map indicates a linear breakdown time is possible if the semiclassical dynamics are developed in a well-adapted representation [20]. If a poorly adapted representation is chosen, then breakdown is immediate. The log time played no real role. The evidence from the stadium, the kicked rotor, and recent theoretical work also supports the conclusion that the log-time concept is overly pessimistic [4, 16]. Furthermore, studies such as that of Christoffel and Brumer [21], though lacking a semiclassical analysis, are suggestive of a longer-time correspondence.

The purpose of this paper is to address the difficult questions about long-time semiclassical accuracy. In so doing we give a complete account of our work on the semiclassical dynamics of the stadium. This study is made more timely by recent experimental interest in the stadium. There are groups measuring properties, such as conductances, of mesoscopic stadium conductors [22] as well as eigenvalues and eigenfunctions of two-dimensional (2D) stadia microwave cavities [23]. Recent interesting connections have been pointed out between the bound and scattering states of such systems [24].

We begin the main text of this paper with a quick overview on semiclassical propagation. In the following section, we give a brief description of properties of chaos necessary for understanding our technique of evaluating the semiclassical propagator. The theoretical difficulties and procedures are described in more detail and finally, classical, quantum, and semiclassical studies are put together for the stadium billiard. It is shown that the agreement extends well past the time that the chaos is highly developed and classical structure far finer than a quantum cell is put into the semiclassical dynamics. We then derive the $\hbar$ dependence of the validity of the semiclassical approximation.

## II. SEMICLASSICAL DYNAMICS

The overriding theme or universal idea behind semiclassical mechanics can loosely be described as approximating quantum amplitudes using the square roots of classical probabilities supplemented by the superposition principle and classically calculable phases. Although easily stated, exacting implementation often requires a lot of care, the existence of a formal mathematical structure notwithstanding. This is especially true here because we are specifically interested in the complications introduced by chaos and longer-time dynamics. We therefore describe in detail the calculational techniques that have been developed. Since they are deeply connected extensions of existing semiclassical approximations, we begin with a review of the material needed to make the discussion self-contained.

### A. The semiclassical approximation

As a starting point, consider a quantum system governed by a Hamiltonian $\hat{H}$. Our basic goal will be to determine to what extent the system prepared in an initial state $|\alpha\rangle$ evolves into some final state of interest $|\beta\rangle$. The overlap of $|\alpha(t)\rangle$ and $|\beta\rangle$ gives the desired correlation function

$$C_{\beta\alpha}(t) = \langle\beta|\alpha(t)\rangle = \langle\beta|e^{-i\hat{H}t/\hbar}|\alpha\rangle \tag{1}$$

and the exponentiated $\hat{H}$ operator is the quantum propagator. Working in the customary configuration-space representation, the propagator becomes the time-dependent Green's function

$$G(\mathbf{q}, \mathbf{q}'; t) = \langle\mathbf{q}|e^{-i\hat{H}t/\hbar}|\mathbf{q}'\rangle, \tag{2}$$

whose construction is formally given by Feynman's path integral [25, 26]. The propagation of a wave function $\Psi_\alpha(\mathbf{q}) = \langle\mathbf{q}|\alpha\rangle$ can then be written as a configuration-space integral

$$\Psi_\alpha(\mathbf{q}; t) = \int_{-\infty}^{\infty} d\mathbf{q}' \, G(\mathbf{q}, \mathbf{q}'; t)\Psi_\alpha(\mathbf{q}') \tag{3}$$

as can correlation functions

$$C_{\beta\alpha}(t) = \int_{-\infty}^{\infty} d\mathbf{q} \, \Psi_\alpha(\mathbf{q}; t)\Psi_\beta^*(\mathbf{q}). \tag{4}$$

One way to obtain the semiclassical version of $C_{\beta\alpha}(t)$ is to apply the stationary-phase approximation to the Feynman path-integral formulation of the Green's-function and the configuration-space $dqdq'$ integrals. In so doing, one first expresses the wave functions in the suitable form

$$\Psi(\mathbf{q}) = \sum_j A_j(\mathbf{q})e^{i\mathcal{W}_j(\mathbf{q})/\hbar}, \tag{5}$$

where $A_j(\mathbf{q})$ is a slowly varying function of $\mathbf{q}$ and any rapidly oscillating phase is captured in the exponential. The argument $\mathcal{W}_j(\mathbf{q})$ is typically a smoothly varying function whose derivative $\partial\mathcal{W}/\partial\mathbf{q}$ gives the local momentum in the wave function $\mathbf{p}(\mathbf{q})$. The index $j$ allows for the possibility of multiple branches contributing at a given $\mathbf{q}$. This leads to a simple prescription for constructing the semiclassical approximation. First, an initial manifold of phase points $\{\mathbf{q}, \mathbf{p}(\mathbf{q})\}_\alpha$ underlying $\Psi_\alpha(\mathbf{q})$ is identified. It is propagated classically a time $t$ and the intersections with the final manifold $\{\mathbf{q}, \mathbf{p}(\mathbf{q})\}_\beta$ identify the classical trajectories that represent the stationary-phase "points" of the theory.

This structure is evident in the VVG propagator [12, 13]. Performing the semiclassical approximation directly to the Green's function leads to

$$G(\mathbf{q}, \mathbf{q}'; t)$$

$$\approx G_{\mathrm{sc}}(\mathbf{q}, \mathbf{q}'; t)$$

$$= \left(\frac{1}{2\pi i\hbar}\right)^{d/2} \sum_j \left|\mathrm{Det}\left(\frac{\partial^2 S_j(\mathbf{q}, \mathbf{q}'; t)}{\partial\mathbf{q}\partial\mathbf{q}'}\right)\right|^{1/2}$$

$$\times \exp\left(iS_j(\mathbf{q}, \mathbf{q}'; t)/\hbar - \frac{i\pi\nu_j}{2}\right). \tag{6}$$

In this expression, the sum over $j$ is for all trajectories connecting $\mathbf{q}'$ to $\mathbf{q}$ in time $t$ and $d$ is the number of degrees of freedom. The determinant plays the role of the square root of a classical probability, and the phase is determined by the classical action $S_j(\mathbf{q}, \mathbf{q}'; t)$ and an index based on the properties of the conjugate points (like focal points), $\nu_j$. $S_j(\mathbf{q}, \mathbf{q}'; t)$ is specified by the time integral of the Lagrangian $\mathcal{L}$

$$S_j(\mathbf{q}, \mathbf{q}'; t) = \int_0^t dt'\, \mathcal{L}$$

$$= \int_0^t dt'\, \{\mathbf{p}(t') \cdot \dot{\mathbf{q}}(t') - H(\mathbf{p}(t'), \mathbf{q}(t'))\} \tag{7}$$

along the $j$th classical path. $H$ is the classical Hamiltonian which is presumed to be the classical limit of $\hat{H}$. Equation (6) was originally written down by Van Vleck in 1928 without the summation or index $\nu$ and was thus fundamentally limited to extremely short times at best. It was Gutzwiller who, much later, worked with the final form above in deriving the trace formula as a sum over periodic orbits.

### B. Wave packets and linearized dynamics

Although $G_{\mathrm{sc}}(\mathbf{q}, \mathbf{q}'; t)$ is formally written down in Eq. (6), it suffers from severe mathematical complications; this is not surprising since a similar statement could be made of the Feynman path integral from which it may be derived. With the complete momentum uncertainty in $\mathbf{q}$ states, trajectories of all energies and complexity must be incorporated. In addition, it is quite

possible, depending on the system, that $G_{\mathrm{sc}}(\mathbf{q}, \mathbf{q}'; t)$ has singularities and divergences everywhere in $\mathbf{q}$ and $\mathbf{q}'$ no matter how small a time investigated. This happens, for example, for potentials that increase sufficiently rapidly, so that high-energy trajectories return arbitrarily frequently at short time. On the other hand, many of the difficulties with $G_{\mathrm{sc}}(\mathbf{q}, \mathbf{q}'; t)$ are not encountered in the propagation of smooth, square-integrable wave functions having finite-energy uncertainties. The wave functions can be thought of as reorganizing or filtering the information in the Green's function. For convenience, we shall focus on wave packets $\Phi(\mathbf{q})$ of the form

$$\Phi(\mathbf{q}) = \left(\pi\sigma^2\right)^{-d/4} \exp\left(-\frac{(\mathbf{q} - \mathbf{q}_0)^2}{2\sigma^2} + \frac{i\mathbf{p}_0}{\hbar}\cdot(\mathbf{q} - \mathbf{q}_0)\right), \tag{8}$$

which allow one to zero in on a localized $(h^d)$ volume of choice in phase space. The region of phase space whose trajectories are relevant to the wave packet can be roughly visualized by taking the Wigner transform $\Phi_W(\mathbf{q}, \mathbf{p})$ of Eq. (8). It is a Gaussian distribution centered at $(\mathbf{q}_0, \mathbf{p}_0)$ with variances $\Delta q^2 = \sigma^2/2$ and $\Delta p^2 = \hbar^2/2\sigma^2$. If $\sigma^2$ is chosen to be real, then the covariance $\Delta qp = 0$, giving

$$\Phi_W(\mathbf{q}, \mathbf{p}) = \frac{1}{\pi\hbar}\exp\left(-\frac{(\mathbf{q} - \mathbf{q}_0)^2}{\sigma^2} - \frac{(\mathbf{p} - \mathbf{p}_0)^2\sigma^2}{\hbar^2}\right). \tag{9}$$

For a $C_{\beta\alpha}(t)$, where $|\alpha\rangle$ and $|\beta\rangle$ are wave packets, the ideal approximation, outlined above, of applying the full method of stationary phase would bring us to the generalized Gaussian wave-packet dynamics of Huber, Heller, and Littlejohn [27]. They established the equivalence of their method to the semiclassical (WKB) approximation in the complex domain. The $\{\mathbf{q}, \mathbf{p}\}$ manifolds of phase points underlying $|\alpha\rangle$ and $|\beta\rangle$ are generally complex. The use of complex classical trajectories is a serious complication and is prohibitive for present purposes. So, we shall back away from the ideal route by holding off on performing the saddle-point (complex stationary phase) method directly to the $dqdq'$ integrals. Instead, the Gaussian wave packets will be weight factors to the real classical orbits contributing to the VVG propagator.

The basic ideas (necessary for including nonlinear recurrences) build upon the well-developed linear wave-packet dynamics [28, 29], so we discuss this first. Suppose that one is interested in short-time dynamics and $\hbar$ is not too large. The classical trajectories that are relevant to the propagation of some $\Phi(\mathbf{q})$ of Eq. (8) are those whose initial conditions are near an $h^d$ volume $d\mathcal{V}$, centered at $(\mathbf{q}_0, \mathbf{p}_0)$ in similarity with the volume "occupied" by $\Phi_W(\mathbf{q}, \mathbf{p})$. The essential nature of the propagation of $d\mathcal{V}$ is seen by following the centroid phase point from $(\mathbf{q}_0, \mathbf{p}_0)$ to $(\mathbf{q}_t, \mathbf{p}_t)$ which is taken as a reference trajectory. The volume $d\mathcal{V}$ is distorted by an approximate local linear transformation generated by the dynamics. The linear transformation is specified by the classical stability matrix as

$$\begin{pmatrix} \partial \mathbf{p}_t \\ \partial \mathbf{q}_t \end{pmatrix} = \mathbf{M}_t \begin{pmatrix} \partial \mathbf{p}_0 \\ \partial \mathbf{q}_0 \end{pmatrix} \tag{10}$$

where $(\partial \mathbf{q}_t, \partial \mathbf{p}_t)$ is the deviation from $(\mathbf{q}_t, \mathbf{p}_t)$ at time $t$ of a trajectory started a small displacement $(\partial \mathbf{q}_0, \partial \mathbf{p}_0)$ from $(\mathbf{q}_0, \mathbf{p}_0)$. The determinant of $\mathbf{M}_t$ is unity by flux conservation (Liouville's theorem). For a stable trajectory, $\mathbf{M}_t$ describes the local shearing or rotation. For an unstable trajectory, $\mathbf{M}_t$ will reflect the hyperbolic nature (exponentially rapid stretching) of the local dynamics. Its eigenvectors will be tangent to an unstable and a stable manifold which are, respectively, the local directions of exponential expansion and contraction. The eigenvalues give the magnitude of the expansion and contraction and give one a good approximate idea of how rapidly $d\mathcal{V}$ becomes wildly distorted.

Linear wave-packet propagation follows by translating the initial wave-packet centroid along the central orbit from $(\mathbf{q}_0, \mathbf{p}_0)$ to $(\mathbf{q}_t, \mathbf{p}_t)$ and applying the unitary transformation to $\Phi(\mathbf{q})$ corresponding to the classical linear transformation $\mathbf{M}_t$ of that orbit. Use was made of a locally linearized version of the VVG propagator to take care of precisely this and ensure the correct phase. The details of the one degree of freedom calculation and Gaussian integrals are given in Appendix A. A slight generalization of the Les Houches lecture notes of one of us [29] is given in which trajectories other than $(\mathbf{q}_0, \mathbf{p}_0)$ may be utilized as the reference; this is a preparation for eventually incorporating the nonlinear dynamics. Note that to the extent that the local dynamics are linear, linear wave-packet dynamics is a way of obtaining a single stationary-phase contribution (without locating the actual point) and is equivalent. If there is some curvature in the local deformation of $d\mathcal{V}$ (curvature in the way the branches slice through the disk), it is necessary to pay some attention to which trajectory is chosen as a reference. Otherwise, any trajectory from the central branch inside $d\mathcal{V}$ serves equally well as the reference trajectory.

The calculation of a classical correlation function is schematically illustrated in Fig. 1, which shows successive snapshots of an evolving group of trajectories. As the group stretches and evolves, recurrences result from branches slicing through the the central region of the unpropagated group—one branch at first, then more and more as time increases. The linear-dynamical approximation of the correlation function accounts only for the central branch. It uses the stability properties of the central orbit as a reference, and gets the weight of the central branch right, but nothing else. Sooner or later, the recurrences of the side branches will dominate the correlation function; their relationship to the central branch is highly nonlinear. By this time, the linearized dynamics fails to properly describe the classical correlation function and therefore the linear wave-packet dynamics description of the recurrences must also fail.

### C. Spectra

Often it is important to seek stationary-state quantum solutions. By using the time-energy Fourier transform, one can "filter" out intensity-weighted spectra from autocorrelation functions, and eigenstates from propagated states. The exact intensity spectrum of an initial state $\Phi_\alpha(\mathbf{q})$ is projected by

$$S(E) = \frac{1}{2\pi\hbar} \int_{-\infty}^{\infty} dt\, e^{iEt/\hbar} C_{\alpha\alpha}(t)$$

$$= \sum_n |c_n^\alpha|^2 \delta(E - E_n),$$

$$\Phi_\alpha(\mathbf{q}) = \sum_n c_n^\alpha \Psi_n(\mathbf{q}), \tag{11}$$

where $\Psi_n(\mathbf{q})$ is the eigenstate at the eigenvalue $E_n$. In the usual case where one does not have access to an infinite-time argument in $C_{\alpha\alpha}(t)$, the energy resolution is degraded to $\delta E = 2\pi\hbar/t_m$, where $t_m$ is the maximum time attainable.

It is worthwhile recalling how much information about $S(E)$ can be obtained from the linear wave-packet analysis. An interesting case is to consider placing $|\alpha\rangle$ somewhere along a short, unstable periodic orbit. Figure 2
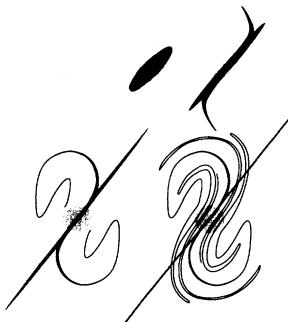


FIG. 1.  A schematic illustration of the hyperbolic structure of phase space. The swarm of trajectories, i.e., the black disk, exponentially stretches apart as time evolves from upper left to lower right. The light gray disks indicate the initial swarm and the medium gray javelin shows the local linear-dynamical approximation.
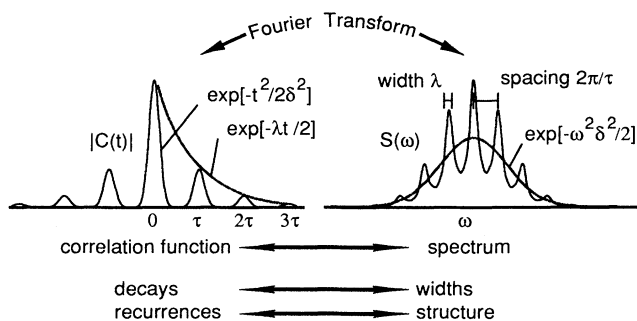


FIG. 2.  The linear dynamics of an autocorrelation function on an unstable periodic orbit and its spectrum. The relationships between the spectral features and the time-domain decay and recurrence scales are indicated. Taken from Ref. [29].

summarizes the overall situation. There is an average rate of the oscillating phase (not pictured) determining the centroid of the spectrum. The decay time of the initial falloff sets the breadth of the envelope. The classical frequency of motion for one cycle of the orbit gives rise to the spacing between peaks. And finally, the broadening of the peaks is determined by the classical orbit's Lyapunov exponent. This level of understanding is sufficient, incidentally, to prove the existence of eigenstate scarring [30]. More details can be found in [29].

There may be many more structures one would like to understand in a spectrum. They will necessarily require learning to include nonlinear dynamics. The spectral structures linked to the linearized dynamics are not destroyed by including the full dynamics. They remain intact. The role of the longer-time dynamics is simply to increase the resolution.

## III. CHAOS

The intricate nature of chaotic dynamics in a bounded dynamical system arises from the interplay of just a few key ingredients. Any subregion in phase space must preserve its volume under evolution while becoming progressively more distorted. The distortion proceeds so rapidly that the majority of the available phase space has been explored in a coarse-grained sense on an extremely short-time scale, logarithmic in the coarse-graining size. This explains the appearance of the schematic dynamics of Fig. 1. The initial volume $d\mathcal{V}$ rapidly transforms into a filamentary object with many branches cutting through the original $d\mathcal{V}$ or any other $d\mathcal{V}$ elsewhere. Due to the exponential spreading and $h^d$ volume of $d\mathcal{V}$, the simple linearized correlation function approximations fail on the logarithmically short-time scale $t^*$. However, since the failure of the linearized wave-packet dynamics is due to getting the classical dynamics wrong and not by some intrinsic problem with the semiclassical approximation, one can hope to do much better.

We must first understand the rudiments of classical correlation functions. Ignoring the question of whether or not semiclassical mechanics should work, the basic problem which must be solved in order to evaluate the semiclassical approximation to $C_{\beta\alpha}(t)$ begins with the purely classical one of organizing and computing the necessary dynamical information. The key classical ideas necessary for making the semiclassical analysis (ahead) feasible can be envisioned by imagining the forward propagation of the initial volume $d\mathcal{V}_i$ a time $t/2$ and the backward propagation of the final volume $d\mathcal{V}_f$, $t/2$. The two filamentary volumes thus produced, if they intersect, will do so in tiny neighborhoods. Each one gives a contribution to the correlation function and is typically well approximated by a local linearization of the dynamics. They are located on "heteroclinic" orbits found at the intersections of certain stable and unstable manifolds of orbits. This is described more generally and in further detail below.

### A. Nonlinear classical reccurences

Consider an initially localized density of phase points $\rho_\alpha(\mathbf{q}, \mathbf{p})$. The classical correlation function $\Gamma_{\beta\alpha}(t)$ formed with a second localized density $\rho_\beta(\mathbf{q}, \mathbf{p})$ is defined as

$$\Gamma_{\beta\alpha}(t) = (\rho_\beta, \rho_\alpha(t))$$
$$= \int d\mathbf{q}\, d\mathbf{p}\, \rho_\beta(\mathbf{q}, \mathbf{p})\rho_\alpha(\mathbf{q}, \mathbf{p}; t), \qquad (12)$$

where $\rho_\alpha(\mathbf{q}, \mathbf{p}; t)$ is determined from the density $\rho_\alpha(\mathbf{q}', \mathbf{p}')$ by associating $(\mathbf{q}', \mathbf{p}')$ to the point that will evolve into $(\mathbf{q}, \mathbf{p})$ in a time $t$. Because our interest in $\Gamma_{\beta\alpha}(t)$ is motivated by wave-packet correlations, we assume that $\rho_\alpha$ and $\rho_\beta$ are localized, Gaussian densities that occupy relatively small fractions of the available phase space, even though this is unnecessary for much of the following picture of the dynamics.

We start with the simple observation that almost every orbit has at finite times a neighborhood of orbits that behaves very similarly. The properties of these nearby orbits, such as their actions, will be approximated fairly well by a low-order expansion about the original orbit. This suggests imagining the phase space as divided into partitions each containing subsets of similarly behaving orbits. In many of the systems used as paradigms of chaos, for example, certain billiards, the partitioning for $t$ not too large is easy to construct. There are also a few chaos paradigms for which the partitioning may be performed analytically for all time. This leads us directly into the subjects of symbolic dynamics and Markov partitions [31]. However, we will refrain from entering these topics and will keep the discussion on an intuitive level.

All the transport properties reflect the partitioning. Each partition of orbits potentially contributes to a correlation function depending upon the initial and final densities, $\rho_\alpha$ and $\rho_\beta$, respectively. Calculating correlation functions reduces first to finding which partitions have an intersection initially with $\rho_\alpha$ and after propagation intersect $\rho_\beta$. It is thus natural to decompose correlation functions into a sum over separate contributions $\gamma$ as

$$\Gamma_{\beta\alpha}(t) = \sum_\gamma (\rho_\beta, \rho_\alpha(t))_\gamma, \qquad (13)$$

where $\gamma$ runs over the partitions at time $t$. This is just an organization of the recurring trajectories and does not yet involve approximation. The second step is to evaluate each partition's weight. The goal is not to perform this exactly, but rather find an approximation scheme that is far simpler to carry out and is motivated by our desire to extend it into the semiclassical realm. For $\rho_\alpha$ and $\rho_\beta$, taken anywhere from most regions of phase space, the propagated trajectories will slice through $\rho_\beta$ in slender, nearly parallel branches as pictured in Fig. 1; a similar inverted image exists for going backward in time. Viewed within $\rho_\beta$, each branch contains the subset of orbits contributing from a particular partition $\gamma$. A great simplification often arises from the linear way in which each branch slices through the final distribution $\rho_\beta$. Nearly all individual $(\rho_\beta, \rho_\alpha(t))_\gamma$ can be approximated exactly as the single contribution in the "old" linear-dynamical picture. To an excellent approximation

$$(\rho_\beta, \rho_\alpha(t))_\gamma \approx \int d\mathbf{q}\, d\mathbf{p}\, \rho_\beta(\mathbf{q}, \mathbf{p}), [T_\gamma \rho_\alpha](\mathbf{q}, \mathbf{p}; t), \qquad (14)$$

where $T_\gamma$ linearly transforms $\rho_\alpha$. The anchoring point of the transformation may be chosen as any trajectory within $\gamma$, however, it is best to select a trajectory which both starts as closely as possible to the center of $\rho_\alpha$ and finishes as closely as possible to the center of $\rho_\beta$. The stability parameters of this reference orbit are used to determine $T_\gamma$, thus approximately including the contribution of the full branch to $\Gamma_{\beta\alpha}(t)$. The more unstable the reference orbit, the "thinner" or "lighter" the branch.

All of the nonlinearities accounted for are in the summation and the full dynamical problem is reduced to one of multiple local linearizations. With $\rho_\alpha$ and $\rho_\beta$ chosen to be Gaussian densities, the integrals in Eq. (14) can be done analytically. The sources of error in the approximation will be due either to local "curvature" or "end-point" corrections. As $\rho_\alpha$ and $\rho_\beta$ shrink both sources of error will disappear for almost all regions of phase space at fixed time.

We now need a method of locating a single reference trajectory from each branch satisfying the above criterion. Of the many possible search techniques for representative trajectories, we developed a method motivated by an interest in Gaussian densities which share their $(\mathbf{q}, \mathbf{p})$ uncertainties, i.e., are not too close to either a $\mathbf{q}$ state nor $\mathbf{p}$ state. A natural way to locate the necessary set of reference orbits is to consider the direction of exponential expansion of $\rho_\alpha$ and the direction of contraction of $\rho_\beta$. Many years ago, Birkhoff introduced a normal coordinate form for analytic mappings applicable to the dynamics in the neighborhood of a hyperbolic invariant point [32]. The convergence was later discussed by Moser [33]. The rough idea applied here is that given a domain of convergence in the neighborhood of the hyperbolic point, all (forward and backward) iterations of the domain, are convergent as well [10]. If $\rho_\alpha$ lies entirely within the initial domain of convergence of its central orbit, the whole density can be thought of as continually collapsing onto an ever increasing portion of the central orbit's unstable manifold $\mathcal{U}_\alpha$. Likewise, the density $\rho_\beta$ propagated backward in time is collapsing onto an ever increasing portion of its central orbit's stable manifold $\mathcal{S}_\beta$. The recurrences are thus necessarily linked to the intersections of $\mathcal{U}_\alpha$ and $\mathcal{S}_\beta$ and tiny neighborhoods about them. At the intersections are heteroclinic orbits. The number of relevant heteroclinic contributions will increase exponentially with increasing time just as the individual neighborhoods shrink exponentially. If $\rho_\alpha$ and $\rho_\beta$ have the same central orbit, the intersections are on homoclinic orbits. The selection of the relevant portion of $\mathcal{U}_\alpha$ and $\mathcal{S}_\beta$ is illustrated in Fig. 3. The ellipse encircling the outer edges, say $3\sigma$ or $4\sigma$, of the Gaussian density are projected down onto the manifold as indicated. Heteroclinic intersections further out on the manifolds could be included but they are damped out by a Gaussian weighting rendering their contributions completely negligible. There will be one and only one heteroclinic orbit per contributing $\gamma$ if the conditions for having the domain of convergence apply (this does not strictly apply to the
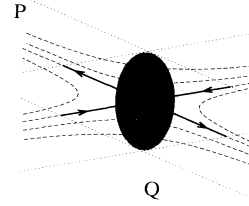


FIG. 3. The relevant portions of the stable and unstable manifolds. The wave-packet's ellipse of uncertainty is projected down onto each manifold along the direction of the other. The relevant manifold sections are indicated in solid black. The ellipse contour corresponding to about $4\sigma$ should suffice in most cases.

stadium, but we can still proceed in Sec. IV as though it does). Because the organization into partitions and the collective contribution of each one's trajectories can be accounted for by a set of heteroclinic orbits along with their stability analysis, we shall usually refer to Eq. (13) (especially in Sec. IV) as a heteroclinic orbit sum even though the partition organization is the more fundamental and correct viewpoint.

We note that an analogous procedure is easily generated for integrable dynamics. Instead of stable and unstable manifolds, one must consider manifolds of trajectories motivated by the structure of the local shearing or rotation of the dynamics; this is straightforward. Less obvious is how to generate the analogous procedure for mixed dynamical regions where there is a complicated coexistence of regular and chaotic motion.

### B. Semiclassical incorporation of nonlinear dynamics

An approximate technique of propagating quantum wave packets can be built on precisely the same concepts as the classical correlation functions. Each partition in a semiclassical evaluation of the correlation function will give a square root of a classical probability and a phase. Since the classical recurrences partition into separate contributions, so too must the semiclassical. The contributing orbits of the partition work together to form a local component wavelet. We can write analogously, therefore,

$$C_{\beta\alpha}(t) \approx \sum_\gamma \langle \beta | \alpha(t) \rangle_\gamma. \qquad (15)$$

Each contribution is determined by evaluating the Gaussian-weighted, configuration-space integrals over the locally approximated VVG propagator; see Eq. (6) and Appendix A. A linearization of the dynamics is used about each of the reference heteroclinic orbits and the basic results of the old linear wave-packet dynamics can be borrowed for each term; the calculation boils down to the computation of the heteroclinic orbits, their actions, stabilities, and phase indices. In this view of the wave-packet dynamics, the previous linear version is recovered for times short enough that only the central partition is significantly contributing and its breakdown occurs as

soon as multiple terms become necessary.

We have in a sense sacrificed the purity of the true stationary-phase approximation, but found an immensely simpler evaluation which closely respects the stationary phase. To the extent that for each heteroclinic branch there exists a complex stationary-phase trajectory, the linearization about the real heteroclinic orbits and ensuing Gaussian integral effectively "locates" these complex trajectories and gives their stationary-phase contribution. As long as the heteroclinic orbit is in the immediate neighborhood of a complex stationary-phase trajectory, there should be only a tiny "curvature" correction between the linearized dynamics of the two points. The difficulty of complex stationary-phase points which do not correspond to branches of real orbits is more subtle and will be treated in another work [34].

## C. The area-$\hbar$ rule

We now have a practical technique for including nonlinear dynamics into semiclassical propagation. In our letter it was shown to be very effective, but little was said as to why it worked. An early, extensive theoretical treatment of how chaos affects the stationary-phase approximation was given in Ref. [18], where it was argued that the semiclassical evolution of a state under chaotic dynamics remains accurate only over an extremely short-time scale, $t^* = O(\ln(\hbar^{-1}))$, which is dubbed the log time (see also Ref. [35]). The reasoning was that by this time or soon thereafter, the problems with caustics become quite severe. The argument goes like this. The propagation of a quantum state is connected via semiclassical mechanics to the propagation of a manifold of trajectories. Assuming the dynamics are chaotic and bounded, the manifold will stretch out exponentially fast, depending on the Lyapunov exponent, and then begin folding back upon itself. The time when pieces of the manifold are found "everywhere" on the scale of $\hbar$ cannot be delayed beyond the log time.

In the vicinity of a fold, the projection of the state into configuration space generally will have two nearby stationary-phase points. Consider an isolated case of two coalescing stationary-phase points as illustrated in Fig. 4(a). In this example, a uniformization of the simple stationary-phase approximation leads to an accurate Airy-function form whose argument depends on the black shaded region in the figure. If this area is large compared with $\hbar$, the leading asymptotic form of the Airy function is good and it approaches the nonuniformized sum of two isolated stationary-phase points. If this area is of the order of $\hbar$ or smaller, the uniformization is essential. Without the uniformization, the standard result blows up as the two stationary-phase points coalesce. This is the "area-$\hbar$ rule" and it gives a rough idea of the domain over which a nonuniformized caustic leads to inaccuracies in the semiclassical approximation. Once folds develop, they proliferate exponentially rapidly, giving rise to a large number of spurious infinities in the wave function. Although one might consider uniformizing a pair of isolated, coalescing stationary-phase points, soon af-
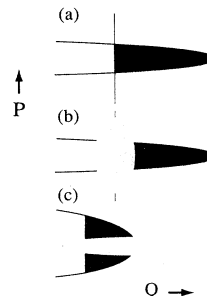


FIG. 4. The area-$\hbar$ rule. (a) The area contained between intersections of the time evolved manifold of a state and a position state (vertical line) is shown as black. If this area falls below $\hbar$, the semiclassical amplitude is in doubt. (b) A coherent state of the type shown is subject to nearly the same area rule. (c) If it is squeezed more like a momentum state, no caustic problems arise.

ter the log time one would be overwhelmed by multiple coalescing points everywhere. The semiclassical approximation appears to be headed for a total collapse in this view.

There are some modifications needed to the area-$\hbar$ logic if the wave function is projected onto localized Gaussian wave packets instead of into configuration space. It is easy to check that if the relationship between the wave packet and the propagated manifold of trajectories is as pictured in Fig. 4(b), the area-$\hbar$ rule remains true, although the divergence will be smoothed out by the Gaussian. The inaccuracies project into the same domain of the wave function as before, but with errors more like a factor of 2 or 3; less if the Gaussian is "momentumlike" for this example. This opens the door, if there are many contributions in a certain region, for the good ones to dominate the inaccurate ones. The breakdown is more tied to the relative fraction of good versus poor contributions than just the existence locally of a single divergent caustic. This can drastically alter one's expectations of the time scale of breakdown; see Sec. IV E. A second point is that the subject of caustics is highly representation dependent. If the wave-packet–manifold relationship is more as pictured in Fig. 4(c), there is no longer an area-$\hbar$ rule to worry about. Both of these considerations tend to chip away at the log-time barrier without violating the fundamental point of the area-$\hbar$ rule. In short, judicious handling of the phase-space dynamics can greatly enhance a semiclassical approximation.

In the baker's map the manifolds are "chopped," leaving no areas to identify for the area-$\hbar$ rule. There semiclassical validity was found to extend to a linear time scale [20]. The stadium also has a kind of discontinuity (see below) even though there is no trouble identifying areas. However, recent work by Sepúlveda and the present authors [16] suggests that the excellent accuracy is a general phenomenon. They show that given the area-$\hbar$ rule $t^*$ still does not spell the demise of semiclassical propagation. We leave the theory aside here and return to the specifics for the stadium later in Sec. IV where a derivation of the breakdown time scale is given.

## IV. THE STADIUM BILLIARD EXAMPLE

The stadium billiard has been an extremely useful tool for studies of chaotic systems from both a classical and quantum-mechanical viewpoint. Bunimovich [36] first proved that it is classically chaotic. A few years later, work on the quantized version began in earnest with McDonald's thesis [37]. They developed a Green's-function technique for obtaining the eigenvalues and eigenvectors, and gave a tremendous impetus to the study of the eigenvectors of classically chaotic systems. Shortly thereafter, the quantized version played a role in the Bohigas-Giannoni-Schmit conjecture of the connection between random matrix theories and spectral fluctuations [38] as well as the prediction and discovery of eigenstate scarring by the least unstable periodic orbits [30]. The stadium's status as a paradigm of chaos was cemented.

Just as in Sec. III, where nearly all of the effort to generate a semiclassical approximation was expended on organizing the classical dynamics, we begin here with a classical study of the the stadium which will complete the majority of the work needed for its semiclassical treatment.

### A. The classical dynamics

The classical stadium consists of a free particle specularly reflecting off hard walls whose shape is pictured in Fig. 5. There is a one-parameter family of stadia specified by $\mu$, the ratio of the length of the straight edge to the semicircular diameter. For $\mu = 0$, the stadium reduces to the integrable circular billiard. For all $\mu > 0$, the stadium is fully chaotic [36]. In our calculations, the diameter equals two, the mass equals one, and $\mu = 1$.

A convenient property of the stadium is that the classical dynamics at any two energies are connected by simple scaling relations. It suffices to study the orbits at a fixed energy ($\|\mathbf{p}\| = 1$) in order to understand the dynamics. Each of these individual orbits is a "geometric parent" of a continuous family of orbits ("geometric family") related by just changing the momentum with which one moves along the parent. The result is a large simplification in the classical and semiclassical calculations. The $\gamma$ summation of Eq. (13) [and Eq. (15)] was over the appropriate heteroclinic orbits at a time $t$. In principle, for any other $t$ a different set of orbits is relevant which

would have to be recalculated. With the scaling property, the sum may be interpreted as being over all geometric parents where fixing the time just specifies a particular geometric family member whose action and stability is easily related to the parent.

The free-particle motion in the stadium is not a great difficulty and can be set aside temporarily. The real story of the dynamics is reduced to the mapping of the sequence of bounces off of the hard walls. The canonically conjugate coordinates of position along the boundary and tangential momentum (Birkhoff coordinates) are pictured in Fig. 5. All the $\gamma$ orbits can be located working strictly from this surface of section. The phase space is a finite height section of a cylinder. Figure 6 shows a typical (ergodic) orbit and its representation in the surface of section. It appears to be randomly filling the map except for small excluded regions near the vertical bouncing motion. The excluded region will shrink away with time eventually.

In Sec. III A we loosely described a partitioning of phase space based on existing subdomains containing similar orbits. In the stadium, any two geometric parents are in the same partition and have similar properties, such as actions and stabilities, as long as they bounce off the same succession of sides, i.e., endcap, straight, endcap, ... , etc. (with the correct rotation sense). Those orbits which divide partitions must strike (with arbitrary momentum) one of the four points where the straight edges meet the semicircles. The delineation of the partitions for a fixed number of bounces $m$ is just a matter of locating all the orbits which after $m, m - 1, m - 2, \ldots$ bounces hit these joints. A simple way of doing this is to follow the manifold of trajectories starting from the joints backward in time $0, 1, 2, \ldots, m$ bounces. Inverting the momenta gives the initial domain of the partition. The relation of the initial and final domains is obtained
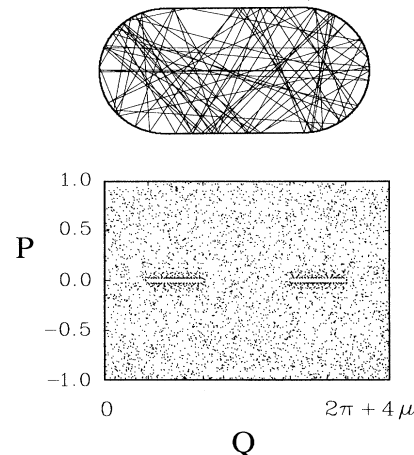


FIG. 6. A typical trajectory. On top is a drawing of an 80 bounce portion of a trajectory started in the neighborhood of the horizontal bounce periodic orbit. Below, the first 4000 bounces of the same trajectory are shown in the surface of section. It appears to fill the surface randomly with the exception of the region of vertical bouncing motion which is sometimes referred to as being "sticky." Eventually the map will be covered uniformly.
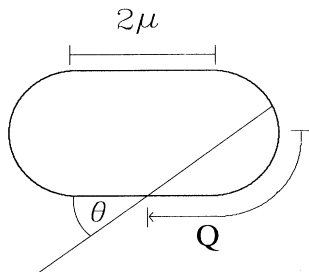


FIG. 5. The map coordinates. The position coordinate $Q$ measures distance along the perimeter moving clockwise from an arbitrary origin, here chosen in the middle of the right semicircle. The momentum coordinate $P$ is the $\cos\theta$ setting the energy equals $\frac{1}{2}$ ($\|p\| = 1$). With the choice of the radius, $r = 1$, the length of the straight edge is $2\mu$.
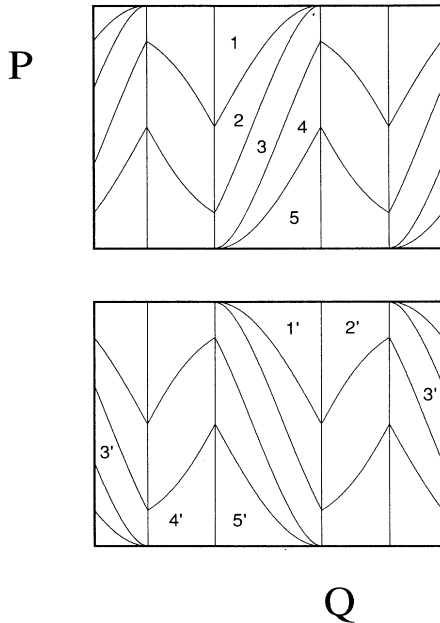
FIG. 7.  The single-iteration partition map.  Each of the delineated regions in the upper figure map into one of the regions in the bottom one.  The numbered regions go into their primed counterparts.

by reflecting the initial one with respect to the $p = 0$ line. The one-bounce partition and its mapping are shown in Fig. 7.  Even with this global symmetry, there is a complicated reordering of the domains by the mapping.  In Fig. 8 the $m = 2$ and 4 initial domains are shown.  The exponential growth of partitioning is striking and is a consequence of the highly chaotic nature of the stadium. By $m = 5$ it is impossible to show the full drawing.

The structure of the partitioning is reflected in propagating a density of trajectories.  After two iterations, the dashed disk of Fig. 9 distorts into the elongated object
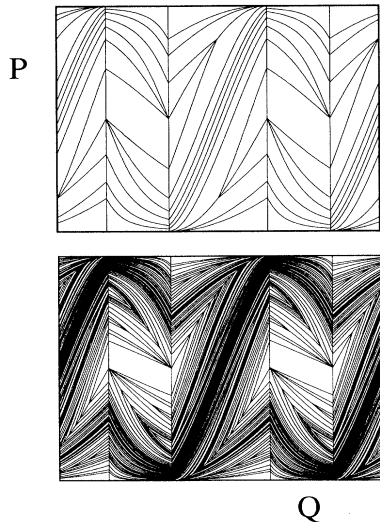


FIG. 8.  The initial domains for the two and four iteration maps, respectively.  The final domains are just the mirror reflections across the middle horizontal line.
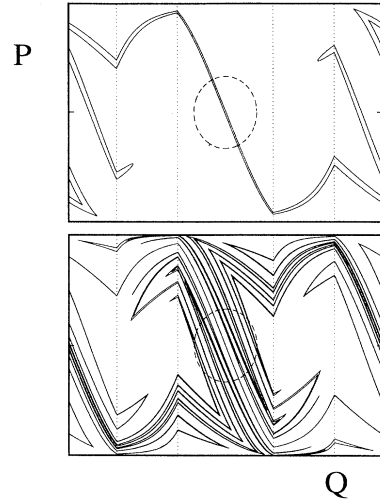


FIG. 9.  Propagation of trajectory swarms.  Pictured are the two and four iteration mappings of the dashed ellipse showing its rapid delocalization.  The dotted lines mark the semicircle–straight-edge joints.

shown in the upper box.  The kinks or folds arise where the initial disk crosses partition boundaries.  After just four iterations in this example (lower box), almost every correlation function would have multiple contributions. The initial branches of phase points propagating into the final branches in $\rho_\alpha$ are shown magnified in Fig. 10.  Typical trajectories from one of the branches are superposed underneath the expanded disk to illustrate how a single branch is capable of supporting a local wave front and that it is related to a single heteroclinic orbit.  All the recurring dynamics of this disk (at just four iterations) is organized by the seven distinct homoclinic geometric parents shown in Fig. 11.  It is important to realize that
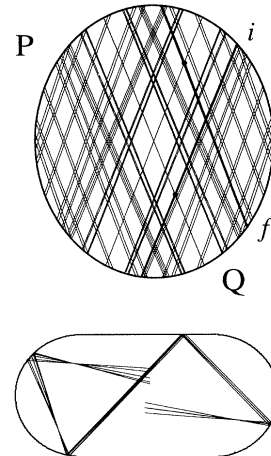


FIG. 10.  Expanded view of the four-times-iterated ellipse of Fig. 9.  The initial conditions of the recurring trajectories are in the right leaning branches which return as the left leaning branches.  The initial conditions darkened and labeled $i$ return as the darkened branch labeled $f$.  Sample trajectories of branch $i \rightarrow f$ are shown underneath.  The homoclinic orbit intersects the black dots on the branches.
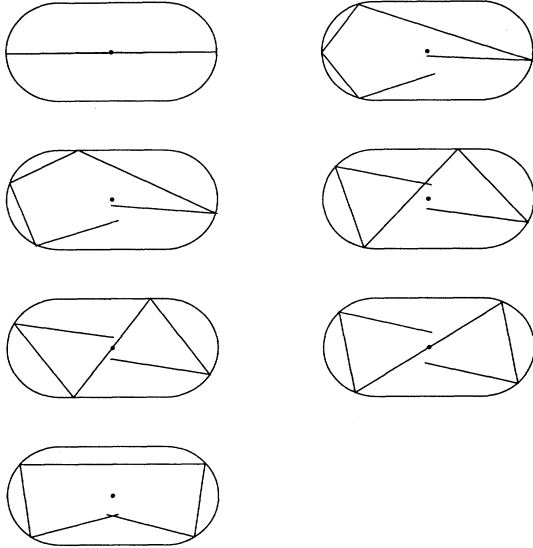
FIG. 11. All the distinct homoclinic trajectories needed to organize the recurring dynamics of the four-times-iterated ellipse. The fourth orbit was the one labeled by $i$ and $f$ in Fig. 10.

all the branches pictured are well within their respective partitions. The boundary of each branch is wholly determined by the cutoffs inherent in $\rho_\alpha$ and $\rho_\beta$. The abrupt boundaries of the partitions are not involved. If one tried to show the same figures for $m = 11$, there would be more than 30 000 filamentary branches slicing through the original circle.

To construct $\Gamma_{\beta\alpha}(t)$ requires connecting the dynamics of the map and its structure to the full dynamics of the stadium, including the free-particle dynamics. The analogous considerations will also be needed later for the semiclassical dynamics. A first point is that the $\rho_\alpha$ and $\rho_\beta$ are taken to lie in the stadium whereas the trajectories found via the mapping dynamics have their initial and final end points on the stadium boundary. The end points need to be extended to the trajectories' closest approach to the $\rho_\alpha$ and $\rho_\beta$ centroids. This occurs where a ray aligned along the coordinate $q_2$ (perpendicular to the orbit) passes through the appropriate $\rho$ centroid. Next, the geometric parents are contributing at all times, $t > 0$. At fixed $t$, only one family member orbit is relevant and it is the one whose momentum along the orbit equals the orbit length divided by the time, $p = l/t$. In $\Gamma_{\alpha\alpha}(t)$, the geometric family thus has a peak contribution time when its family member's momentum best matches that of $\rho_\alpha$. There is a falloff away from this peak depending upon the momentum uncertainties involved.

For each geometric parent, the local stability analysis is most conveniently performed in the coordinate system of the trajectory. The motion along the orbit is free-particle dynamics and is decoupled from the stability analysis in the coordinate perpendicular to the orbit. This simplifies the Gaussian integrations into two separate ones providing that $\sigma^2 = \sigma_{q_1}^2 = \sigma_{q_2}^2$. The overall contribution of a geometric family to the autocorrelation function is just the product of the two.

The parallel direction stability matrix is the free-

particle result of

$$\mathbf{M}_\parallel(t) = \begin{pmatrix} m_{11} & m_{12} \\ m_{21} & m_{22} \end{pmatrix} = \begin{pmatrix} 1 & 0 \\ t & 1 \end{pmatrix}. \qquad (16)$$

For the perpendicular direction, the geometric parent picks up successive multiplicative factors for traveling freely distances $l_i$ across the stadium which alternate with factors from colliding with the walls. One has ($i = 1$ is the rightmost in the multiplication order)

$$\mathbf{M}_\perp = \begin{pmatrix} 1 & 0 \\ l_{n+1} & 1 \end{pmatrix} \prod_{i=1}^{n} \begin{pmatrix} -1 & 2/R\sin\theta_i \\ 0 & -1 \end{pmatrix} \begin{pmatrix} 1 & 0 \\ l_i & 1 \end{pmatrix}. \qquad (17)$$

The $\theta_i$ are the incidence angles of the $i$th bounces defined in Fig. 5 and the radius of curvature $R$ is 1 for the endcaps and $\infty$ for the straight edges. $\mathbf{M}_\perp(t)$ for a given family member is obtained from its parent $\mathbf{M}_\perp$ by dividing the $m_{21}$ element by $p$ $(= \sum_i l_i/t)$ and multiplying the $m_{12}$ element by $p$.

Figure 12(a) shows the heteroclinic orbit summation evaluation of $\Gamma_{\alpha\alpha}(t)$ where $\rho_\alpha$ is aimed directly into one of the endcaps. Although the orbits display an array of complex behaviors, only a few features remain in $\Gamma_{\alpha\alpha}(t)$. There is an initial decay and horizontal bouncing periodic orbit recurrences that rather quickly give way to a fairly flat asymptotic value (a power-law decay correction due to vertical bouncing motion slightly modifies this picture). An interesting result of the heteroclinic analysis is that each geometric family gives an extremely similar shape contribution with time; see Fig. 12(b). Only the overall amplitude and time scales enter. The dashed curve in Fig. 12(a) is the absolute value of the corresponding quantum correlation function, $C_{\alpha\alpha}(t)$. Their correspondence and large differences are discussed below.
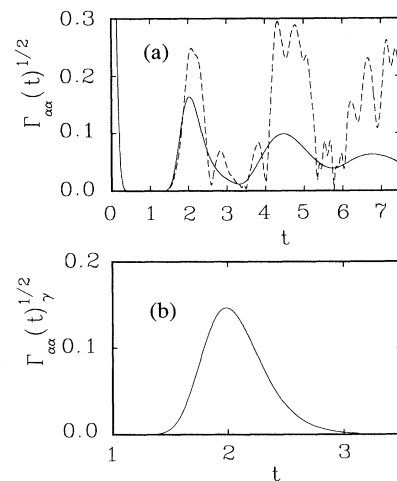


FIG. 12. The classical autocorrelation function. The square root of the classical function is pictured in (a) as a solid line. The absolute value of the corresponding quantum amplitude is superposed as the dashed line. A single homoclinic family contribution is shown in (b). The initial state is the same as in Figs. 14, 17, and 18. Note that $t = 1$ (throughout the figures) is the time to cross the stadium horizontally at the mean momentum; also $m = 1$, $\hbar = 1$, and we use the "2×4" stadium.

Of the two possible sources of error in the heteroclinic sum, curvature of the branches is clearly negligible as is visible from Figs. 8 and 9. The remaining source, that of branches folding abruptly within the boundary of $\rho_\alpha$, is also negligible at short times, but may become more important at longer times. Ahead in the semiclassical heteroclinic sum for $C_{\alpha\alpha}(t)$, this folding is a more severe problem because it is connected to diffraction in the quantum system. It is eventually responsible for breaking down the approximation. See Sec. IV E.

### B. The quantum dynamics

The motion of a quantum particle in a stadium enclosure is governed by the time-dependent Schrödinger equation. Most often Dirichlet boundary conditions are chosen so that wave functions vanish at the walls. However, we find it interesting and necessary for numerical reasons to introduce "soft walls" that allow the quantum particle to penetrate the walls a short distance; this may be the physically relevant situation as with electrons injected into mesoscopic devices. Instead of having an infinitely high potential barrier, the potential is taken to step up from 0 to $V_0$ at the boundary. The classical trajectories below $V_0$ are unaffected by this change. The Dirichlet conditions are recovered in the limit of $V_0/\langle \mathbf{p}^2 \rangle \to \infty$. There are separate reflection symmetries with respect to the central vertical and horizontal axes. A very accurate, fast-Fourier-transform (FFT) technique described in Appendix B is used to propagate states. Special attention was paid to the accuracy in large part because the semiclassical approximation is proving to be so good.

The highly chaotic nature of the stadium is revealed in the propagation of initially localized states. Almost any $\Phi(\mathbf{q})$ will rapidly delocalize and appear to fill the stadium with random-looking waves somewhat akin to the surface of a swimming pool in use (weak-localization effects would normally not be that visible to the naked eye here); see Blumel et al. [39] who, in fact, set up stadium water wave experiments. The most significant exception to the random-looking wave scenario is for a $\Phi(\mathbf{q})$ undergoing the marginally stable vertical bouncing motion.

Shown in Fig. 13 are the contours of the real part of a wave packet initially located at the center of the stadium moving toward the right. Scaling the time for the wave-packet's horizontal traversal of the stadium to be $t = 1$, the propagated wave function is shown for $t = 0, \frac{1}{2}, 1, 2, 6$. By $t = 2$, the time of the shortest unstable periodic orbit, the wave function has already passed the "Ehrenfest time," i.e., it is no longer recognizable as having originated from a localized state. The obvious quantum-classical correspondence time has already passed. The challenge posed by having underlying unstable motion is readily apparent.

The gross behavior of the autocorrelation function $C_{\alpha\alpha}(t)$ is easily understood. Its magnitude will begin at one and drop to nearly zero as the propagated wave packet begins to move away. It will remain nearly zero until $t \approx 2$ when parts of the wave packet will have had
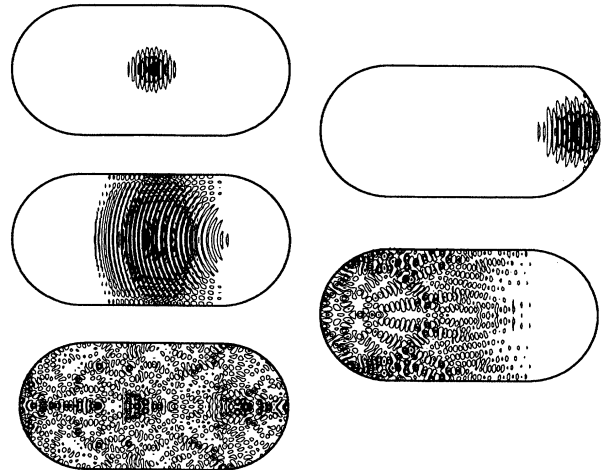


FIG. 13. The quantum propagation of an initial coherent state. Four equally spaced contour lines of the real part of the wave function are plotted in successive time snapshots at $t = 0, \frac{1}{2}, 1, 2, 6$ (moving from upper left to lower right).

the time to travel back and forth across the stadium and generate partial recurrences. Soon thereafter the quantum propagated state seems to be everywhere and $C_{\alpha\alpha}(t)$ will settle into some fluctuating pattern. This is borne out in Fig. 12(a) by the dashed (exact quantum) curve. It is instructive to compare it to the classical equivalent, $\Gamma_{\alpha\alpha}(t)$. The interference oscillations inherent in $C_{\alpha\alpha}(t)$ lead to some large differences between the two. In addition, $C_{\alpha\alpha}(t)$ recurrences look overall significantly stronger than their classical counterparts. This can be accounted for because of coherences related to the discrete reflection symmetries of the stadium.

The counterpart in the energy domain of the complicated interference fluctuations is a spectrum with a great deal of fine structure as is seen in Fig. 14; it is found
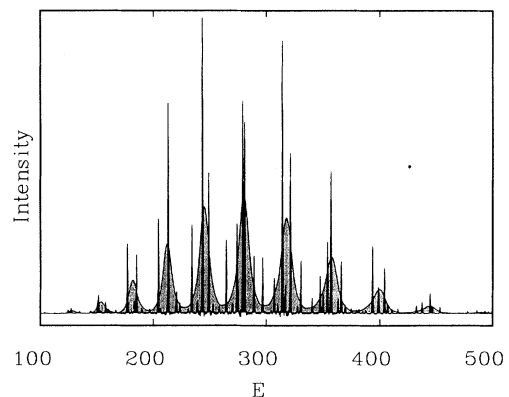


FIG. 14. The quantum intensity spectrum compared to the linear-dynamical prediction. The spectrum roughly spans the 100th to 500th levels (including all symmetry sequences); only the $\{+, -\}$ levels contribute here. The black is the quantum curve and the gray is from the linear dynamics. The widths in the quantum-curve result from our stopping the propagation after a certain length time.

by Fourier transform of the $C_{\alpha\alpha}(t)$. It corresponds to an initial state similar to the one of Fig. 13 except its wavelength is double [as in Fig. 12(a)] and it is anti-symmetrized with respect to reflection about the vertical symmetry line (the state is already symmetric with respect to the horizontal symmetry line). Superimposed on the figure is the linear-dynamical prediction. It roughly locates the regions of maximum and minimum overlap (where the scarred and antiscarred states, respectively, to the horizontal periodic orbit must be located), but it is unable to resolve any further structure.

## C. Conjugate point and soft-wall phase shifts

The great majority of the work involved in producing a semiclassical prediction for stadium correlation functions is already completed by just understanding the classical dynamics as discussed in Sec. IV A and performing the integrals required by Eq. (15). Using the coordinate system described in that section and wave packets of the form Eq. (8), the semiclassical treatment decomposes into free motion parallel and unstable motion perpendicular as did the classical version. The $\gamma$ terms can be thought of as arising from a method of images, one per heteroclinic orbit. The integral of Appendix A is easily adapted to each component by plugging in the heteroclinic orbit and the matrix elements of $\mathbf{M}_{\parallel}(t)$, and $\mathbf{M}_{\perp}(t)$, respectively.

The only task remaining in completing the semiclassical approximation is to calculate $\nu_j$ by keeping track of the $-\pi/2$ phase shifts that arise from passing through conjugate points and by treating the phase shifts of reflecting off soft walls. The conjugate points due to the free-particle dynamics are easily counted by comparing the sign of the $m_{12}$ stability matrix element for the transverse motion. If it changes sign somewhere between reflections off the walls, the unstable manifold has passed through the vertical in phase space. A $-\pi/2$ phase shift is counted; note that no more than one conjugate point may be encountered in traversing the interior. A sign change is possible only after hitting one of the semicircular endcaps.

The soft-wall phase shifts are more complicated. They generate both real and imaginary contributions to the phase in correlation functions. These phases originate in the penetration depth of the local wave which is determined by the wave momentum perpendicular to the wall; momentum parallel to the wall plays no role. The various orbits within one partition do impact the walls slightly differently, but we will ignore this and consider only the reference heteroclinic orbits.

To derive the phase shift it is convenient to begin with a one-dimensional (1D) system of a particle reflecting off a step barrier. The semiclassical eigenstates are exact, assuming the complex trajectory under the barrier is accounted for. Let $V$ denote the energy to climb the step, $m$ the particle mass, and $p_\perp$ the momentum ($\perp$ indicates perpendicular impact for use later in two dimensions). The eigenstates in the classically allowed region are (the step is placed at $q = 0$)

$$\Psi(q) = e^{ip_\perp q/\hbar} + e^{-ip_\perp q/\hbar + i\theta(p_\perp)}$$

$$e^{i\theta(p_\perp)} = -1 + \gamma^2 - i\gamma\sqrt{2 - \gamma^2}, \quad \gamma^2 \leq 2 \qquad (18)$$

where $\gamma^2 = p_\perp^2/mV$ and $E = p_\perp^2/2m$. The incoming initial and outgoing final states are taken to be localized away from the step. They thus have Gaussian amplitude overlaps with the eigenstates equal to their respective Fourier transforms into the momentum representation. In this representation the propagator only introduces a time-varying phase $\exp\left(-ip_\perp^2 t/2m\hbar\right)$ in the overlap integral. Without the phase shift, performing the Gaussian integration exactly equals the stationary-phase approximation and gives the free-particle propagation result. It is good enough for our purposes to treat $e^{i\theta(p_\perp)}$ as a slowly varying function compared with the rest of the integrand so long as the energies of the contributing trajectories do not approach the barrier height too closely. The phase shift is then time dependent and obtained by inserting the stationary-phase condition

$$p_\perp = \frac{q_\beta - q_\alpha}{t} + \frac{p - \frac{q_\beta - q_\alpha}{t}}{1 + it\hbar/2m\sigma^2} \qquad (19)$$

into the relation for $\gamma$; $p \ (= p_\beta = p_\alpha)$ is taken to be equal for the initial ($\alpha$) state and final ($\beta$) state. $p_\perp$ becomes real at the time that an orbit's contribution peaks out in the correlation function. For the stadium, the total phase shift is the product of the individual ones coming from each bounce. A multiplication with the cosine of the incidence angle is included to project out only the perpendicular component of the momentum.

Equation (18) tells us that the soft-wall phase shifts only slowly approach the Dirichlet or hard-wall result of $-\pi$ as the ratio of the barrier height to the trajectory energy approaches infinity. With the multiple bounces of the longer orbits, the differences between hard and soft walls are sufficient to change markedly the details of the interference patterns, even in cases where the penetration depth of the exponentially weak wave-function tails outside the walls are a small fraction of a wavelength.

## D. The semiclassical results and validity

The initial surprise reported in [4, 15] is that every detail of the fluctuating quantum behavior is captured by the semiclassical prediction well past the log time. Superposed in Fig. 15(a) is a solid curve representing the semiclassical $C_{\alpha\alpha}(t)$ and a dashed curve representing the exact quantum solution, showing the excellent agreement. The centroid energy of $\phi_\alpha(\mathbf{q})$, shown in Fig. 13, was chosen so that 30 wavelengths ($\lambda$) span the stadium horizontally. In Fig. 15(b) just the real part of $C_{\alpha\alpha}(t)$ is shown on an expanded scale to display the quality of agreement better. In performing the homoclinic (for autocorrelation functions) summation to obtain the semiclassical prediction, about a dozen geometric parents were contributing at any given time near $t \approx 2$ to 3. By $t \approx 4$ to 5, several hundred were contributing, and by $t \approx 5$ to 6, more than 30 000 geometric parents were needed. To picture the dynamical complexity, recall the bottom right image of Fig. 1 which shows seven branches slicing through the gray disk. To attain $t \approx 5$ or 6, one would have to draw
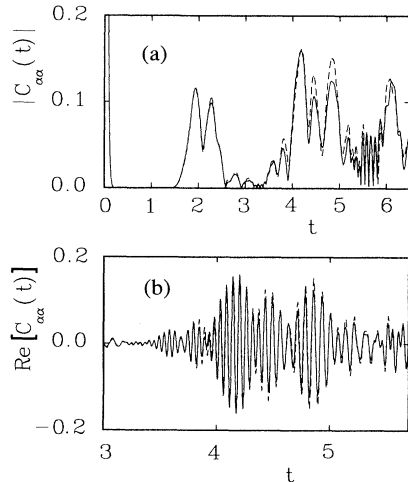
FIG. 15. Comparison of the quantum and semiclassical autocorrelation functions. The solid line is the exact quantum found by a FFT, and the dashed line is the semiclassical approximation. In (a) the absolute magnitude is depicted, and in (b) a view of an expanded piece of the real part is shown.



FIG. 17. The quantum and semiclassical autocorrelation functions for a wave packet centered at half the momentum (or double the wavelength).

more than 30 000 isolated branches fitting in the gray disk. Other than for the beginning of the first recurrence, no individual orbit comes anywhere close to generating the magnitudes of the recurrences seen; all of the terms are necessary. Figure 16 shows an important geometric parent and its family's contribution, $\langle\Phi_a(0)|\Phi_b(t)\rangle_\gamma$. Also shown is a superposition of a number of the neighboring orbits belonging to the same partition whose contributions are included collectively with this parent. The focal points and the local "wavelets" they support are quite visible. The overall shape of $\langle\Phi_a(0)|\Phi_b(t)\rangle_\gamma$ has been found to be quite independent of the particular
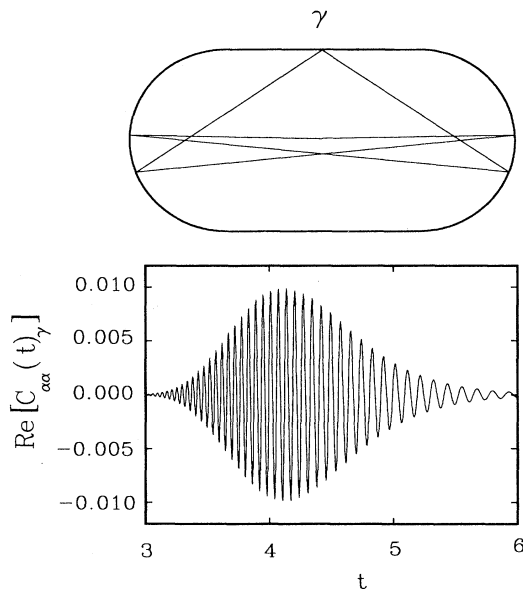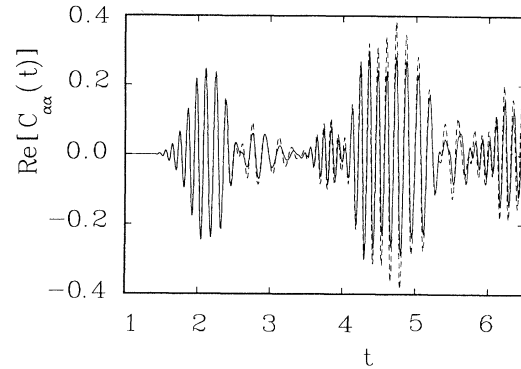
heteroclinic guiding orbit $\gamma$. Note that the scale of its magnitude is much smaller than found in the full sum pictured in Fig. 15.

An important question is whether or how the fundamental approximation fails if $\hbar$ is not sufficiently small. Figure 17 compares a second example where the stadium measured in wavelengths is only $7\frac{1}{2}\lambda$ high by $15\lambda$ long [as in Fig. 12(a)]. We could not increase $\hbar$ much more than this and still handily satisfy the "Birkhoff convergence condition" in the neighborhood of the central trajectory that was mentioned in Sec. III A [32, 10]. We would then need a more sophisticated technique of locating trajectories, perhaps involving complex dynamics. The agreement has degraded somewhat but is still quite good. Evidently, semiclassical behavior does not require exceedingly small $\hbar$.

The overlap intensity of $\Phi_\alpha$ with the eigenstates may be obtained by Fourier transforming the dynamics; see Eq. (11). Figure 18 shows the comparison of the semiclassically derived spectrum with the exact quantum intensity spectrum. The maximum peak occurs near the 300th eigenvalue. Remarkably, the semiclassical theory is reproducing the quantum fine structure to about the scale of a mean spacing. The limit of resolution results from the present practical limit of performing the classical dynamics and not by any failure of the semiclassical dynamics. By $t \approx 8$, $\sim 10^6$ heteroclinic orbits are needed. We have hit the "exponential wall" of orbit prolifera-



FIG. 16. An important primary homoclinic orbit is drawn above its family's contribution to the correlation function of Fig. 14.


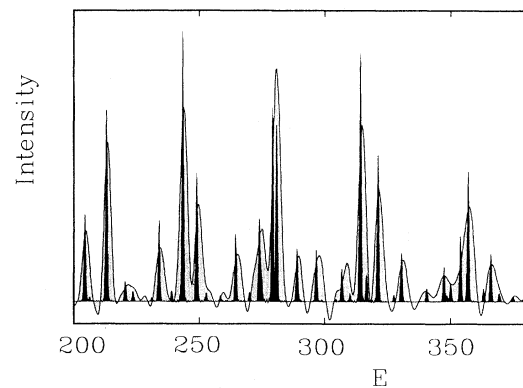
FIG. 18. The middle half of the $\{+,-\}$ spectrum compared with the full semiclassical theory.

tion. It is clear that details are being washed away classi-
cally (recall the simplicity of Fig. 12) and semiclassically
in summing heteroclinic trajectories and their neighbor-
hoods to obtain a simple correlation function. Work is
in progress to identify that information which remains
or how to summarize the classical detail well enough to
break through the wall.

### E. The time scale of breakdown

The dynamics of free propagation and reflection is
clearly handled extremely well semiclassically even for
very long times. A homoclinic orbit like the one pic-
tured in Fig. 16 is a good example. All the related or-
bits and their contributions found by extending this same
basic orbit to longer and longer lengths will also be ac-
curately reproduced. Errors arise though when a wave
(or classical orbit) approaches too closely one of the four
straight-edge–endcap joints. Wave amplitude impinging
there generates diffraction, which is not a part of the het-
eroclinic summation scheme we have introduced. This
occurence is related to a discontinuous fold appearing in
the manifold of trajectories. The classical approximation
also suffers from folding, but only locally (only if the
fold is inside $\rho_\alpha$). In contrast, the effect of folding in the
quantum mechanics is more severe because it is nonlocal.
Folds well away from $\rho_\alpha$ may still give rise to corrections
to $C_{\alpha\alpha}(t)$ in addition to the local foldings.

We now examine the errors due to diffraction more
closely. Consider the elementary process of reflecting an
initial wave packet off the straight edge near the joint
once. The geometry is pictured in Fig. 19. Depend-
ing upon whether $\phi_\alpha$ and $\phi_\beta$ are placed such that the
central trajectory just strikes either the straight edge or
the endcap, the linearized-dynamics prediction disconti-
uously changes, yet the quantum-mechanical amplitudes
are continuous. Figure 20 shows this difference, which
mainly affects the magnitude in this example. The quan-
tum result is found to lie about halfway between these
extremes. It is seen, however, that the respective semi-
classical approximations rapidly become accurate as $\phi_\alpha$
and $\phi_\beta$ are shifted to move the central trajectory away
from the joint. An interesting effect is that the leading
edge of the overlap, which involves the higher momentum
trajectories (shorter $\lambda$), recovers more quickly than the
tail (as should be expected).

It is possible to arrive at a semiquantitative theoreti-
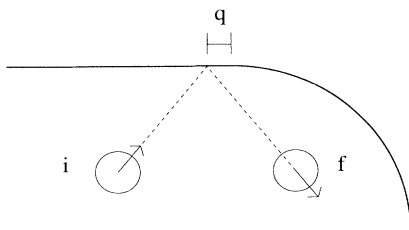cal explanation of the correlation function's behavior in a

FIG. 19. A propagated wave packet starting off in the
direction of the arrow is overlapped with another located at $f$
pointing in the direction of its arrow. $q$ measures the distance
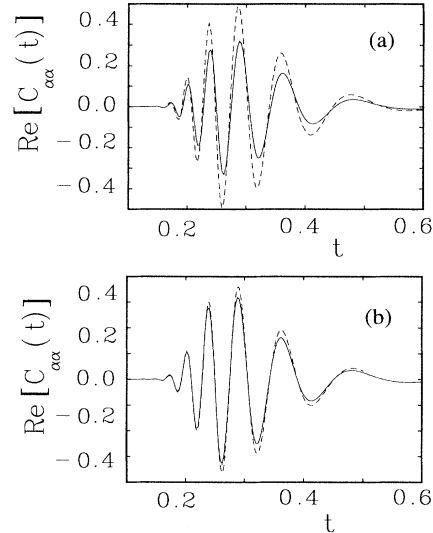by which the classical orbit of the center (dashed line) misses
the joint.

FIG. 20. Accuracy of the semiclassical prediction. In (a)
the discontinuous difference in the semiclassical prediction is
shown. The solid line results in bouncing from the straight
edge and the dashed line from the endcap. The quantum
result roughly lies halfway between the two (not pictured).
In (b) the semiclassical prediction (solid) is compared to the
quantum solution (dashed) when $q$ is $\frac{2}{5}$ of a wavelength (to
the straight-edge side).

straightforward manner. Let us start by freely propagat-
ing an initial wave packet $\phi_\alpha$ toward a hard wall. Along
the wall at any time $\tau$, the wave function must vanish. A
simple approximation is to use the wave magnitude and
phase to "light up" time Green's-function sources giv-
ing a Huygen's-like principle for the construction of the
reflected wave; a wall phase shift may also be included.
Similarly, let a final wave packet $\phi_\beta$ be back propagated
to the wall a time $-(t - \tau)$, generating a different wall
source illumination. The correlation function is reduced
to a time convolution and line integral along the bound-
ary. Diffraction is introduced in the stadium because the
straight-edge line integral stops at the joint and continues
along the curve whose stability parameters are different.
Let $\Phi_1$ be the straight contribution having an appropri-
ate endpoint. Relative to the result of the infinite plane
wall $\Phi$ [which would reflect the content of Eq. (15) eval-
uated within the local linearization approximation], we
find

$$\frac{2\Phi_1}{\Phi} = 1 + \mathrm{erf}(z),$$

(20)

$$z = \frac{p_\perp q}{p\,(\sigma^2 + it\hbar/2)^{1/2}} = \frac{q\sin\theta}{(\sigma^2 + it\hbar/2)^{1/2}},$$

where $p_\perp$ is the transverse momentum at the wall and $q$
is the positive distance between the joint and the clas-
sical orbit connecting the initial and final states. For
$\mathrm{Re}(z) \geq 1$, the relative semiclassical errors are quite
small, $\leq 10\%$ and by scaling $\sigma^2$ as $\hbar$, $z$ can be made to
scale as $\hbar^{-1/2}$. This is consistent with the rapid switch
over with increasing $q$ illustrated in Fig. 20 and provides
additional information as to how the angle of incidence
of the incoming wave enters the problem.

We ignored the wavelet that is emanating from the end-cap. In this case, it would typically reduce the estimate of the error in this example. However, it can be shown that the $\hbar$ dependence of the error is left unchanged. Since we are interested in the case where the radius of curvature does not significantly exceed all the other length scales in the problem, the endcap wavelet is justifiably and safely ignored for our purposes.

We can make a closer connection between this simple single bounce example and multibounce orbits with a few simplifying assumptions. If the initial state is not aimed directly at a joint, by the time a wave makes it there, it is locally behaving much like a plane wave. The errors introduced are largely independent of the complexity of the path leading up to that point. The analogous result to Eq. (20) for the incoming plane wave is just to modify its error function argument $z$ to

$$z = \frac{q\sin\theta}{(\sigma^2 - iq_\perp \hbar/p_\perp)^{1/2}}. \tag{21}$$

$q_\perp$ is the perpendicular component of the wave-packet final-state's centroid. A similar kind of argument could be made in the time-reversed direction. Since it hardly matters whether the close approach to the joint occurs on the fourth bounce or 15th bounce, it suffices to search for a long orbit's minimum value of $q\sin\theta$ to know how trustworthy its semiclassical contribution will be. There is some difference between bouncing off the straight edge and the endcap in this regard, but for our purposes it can be ignored.

A simple probabilistic argument then gives a time scale for the semiclassical breakdown. The accuracy will depend upon the relative fraction of the heteroclinic orbits that remain out of the "troublesome zones" in phase space relative to their total number. We ignore initial transient effects and assume that the orbits of interest are long enough that they "randomly" explore phase space. The small relative phase-space volume that the trajectories must avoid is in the neighborhood of those points which satisfy $q\sin\theta \leq c(t)\hbar^{1/2}$. $c(t)$ is a "constant" that may weakly depend upon time due to the trapping of trajectories near the vertical bouncing ball motion. We find the small volume to be proportional to $\hbar^{1/2}\ln\{c(t)/\hbar\}$; the natural logarithm comes from the whispering gallery motion. In a Markovian picture, the fraction of trajectories avoiding this volume is

$$f = \exp[-\alpha\lambda t\hbar^{1/2}\ln\{c(t)/\hbar\}], \tag{22}$$

where $\alpha$ is a system-dependent constant and $\lambda$ the Lyapunov stability. Thus the time scale of breakdown is roughly $\hbar^{-1/2}$ and not $\ln(1/\hbar)$. The general picture is roughly confirmed with the correlation function of Fig. 17 for which we calculate both the contributing intensity-weighted mean minimum $q\sin\theta$ (adjusted slightly to accomodate the changing momentum of a geometric family's contribution with time) and the intensity-weighted relative fraction avoiding a $q\sin\theta$ of less than half a wavelength; see Fig. 21. Once the statistical relaxation time is reached, the weighted average of $q\sin\theta$ uniformly de-
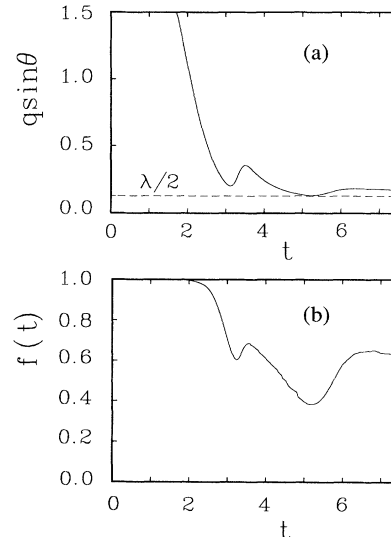


FIG. 21. The proximity of guiding orbits to the joints. In (a) the mean intensity weighted $q\sin\theta$ has some structure as the initial state relaxes. At long times (longer than we could show), it is expected to decrease slowly. The dashed line indicates the scale of half a characteristic wavelength, $\lambda/2$. In (b) is the mean intensity weighted fraction $f(t)$ of the orbits "avoiding" the joints by at least the wavelength scale $\lambda/2$. It also has a similar relaxation time with some structure, but must tend asymptotically to zero.

creases toward zero inversely with $t$. The tendency of the longer and longer orbits to approach the joints is fairly slow. Letting $\hbar$ decrease does not strongly affect the curves. Instead, the $\lambda/2$ line lowers, sending its intersection with the mean-weighted $q\sin\theta$ curve out to much longer times. Thus, the semiclassical time regime grows far faster than $t^*$.

The key lesson is that a standard analysis of semiclassical errors does not necessarily lead to a log-time breakdown for a chaotic system and may extend to a much longer time scale. Although some of the details are not the same due to differences in the phase-space structures (e.g., discontinuous derivatives in the manifolds versus continuous ones generically and in the kicked rotor), it is consistent with the findings of Sepúlveda, Tomsovic, and Heller [16]. Since the classical fine structure in phase-space dynamics develops exponentially fast, extraordinarily detailed classical information can often be trusted to generate excellent approximations to quantum problems without invoking a "magical" explanation (such as "the many errors being made just happen to cancel"). On the other hand, the news is not all optimistic. The derived time scale is not long enough to resolve individual eigenstates and eigenvalues in the semiclassical limit; this has been a major goal since efforts began on understanding the semiclassical dynamics of chaos (and is the goal of periodic orbit theory).

## V. DISCUSSION AND CONCLUSIONS

We have shown that the venerable VVG Green's function, which is the fundamental semiclassical object in

the time domain, is remarkably computable and remarkably accurate, even using detailed classical dynamics with structures on scales far sharper than a Planck cell. Because our method approximates $G_{sc}(\mathbf{q}, \mathbf{q}'; t)$, the already quantitative results could only improve if a better evaluation of the semiclassical dynamics were available. Nearly all the thousands of branches of trajectories are *individually* generating accurate contributions to $C_{\alpha\beta}(t)$; nearby branches do not compromise the accuracy of a given branch. Furthermore, it is not necessary to invoke exotic explanations to understand this accuracy. Standard arguments suffice if carefully applied to the chaotic phase-space structure.

The correspondence principle for chaotic systems extends far beyond the evident initial pre–"Ehrenfest time" regime. The breakdown time-scale arguments, though, do suggest that individual eigenvalues and eigenstates are semiclassically out of reach in the $\hbar \to 0$ limit (unlike their counterparts in integrable systems). Because the density of states for the two-dimensional billiard goes as $\hbar^{-2}$, the time needed to resolve eigenstates scales as $\hbar^{-2}$. Since the derived time scale of accuracy is roughly $\hbar^{-1/2}$, we should not be getting enough information to resolve them individually. In higher dimensions, the situation gets worse. Nevertheless, we saw in Fig. 14 that the semiclassical dynamics could resolve the spectrum to about a mean spacing or so in the energy regime of the 200th to 500th levels. Furthermore, the resolution was limited by hitting the exponential wall of having too many orbits to calculate and not because the approximation began to fail. Where it completely falters has not yet really been found. Our derivation of the time scale for breakdown is apparently still too pessimistic.

It seems that the lack of attention devoted to the semiclassical time Green's function resulted from an overly bleak prognosis of its utility and accuracy. To this one must add the ever present bias against the time domain where pure state quantum mechanics is concerned, a bias which is now rapidly dissipating.

There are many physical phenomena which are best calculated in the time domain. Whenever the "essential physics" is short time or now medium time, it may be best to do calculations in the time domain. This holds true even if the formalism is normally cast in the energy domain. Examples include many types of particle scattering, absorption and Raman spectroscopy, and pulsed-laser experiments. For this reason alone a good semiclassical propagator is needed. Even if one is interested in the energy domain explicitly, it is available from the time domain by explicit (or stationary-phase) Fourier transform.

We are excited by these results because the realm of potential applicability is so large (after all, we are talking about the fundamental quantum propagator), and because there is so much to do to understand these new aspects of semiclassical approximation. We need no longer be concerned that classical chaos puts semiclassical methods out of business.

The doors have been opened on a number of new and old questions which we are pursuing. Summarizing the surviving classical dynamical information so the incredible classical detail is appropriately preprocessed seems possible. The morphology of scarred eigenfunctions can now presumably be much better treated than before, since both our and Bogomolny's theories for the scars were based solely on the linearized dynamics in the vicinity of a periodic orbit. We can now include the nonlinear effects. Diffraction looms as a generic problem in the longtime dynamics. Our methods ignore diffraction, and some reasonable means of incorporating it while maintaining simplicity needs to be invented.

## ACKNOWLEDGMENTS

## APPENDIX A: LINEAR WAVE-PACKET GAUSSIAN INTEGRALS

Let the one degree of freedom Gaussian wave packets be denoted

$$\Phi_\alpha(q) = \left(\pi\sigma^2\right)^{-1/4} \exp\left(-\frac{(q - q_\alpha)^2}{2\sigma^2} + \frac{ip_\alpha}{\hbar}(q - q_\alpha)\right) \tag{A1}$$

and

$$\Phi_\beta(q) = \left(\pi\sigma^2\right)^{-1/4} \exp\left(-\frac{(q - q_\beta)^2}{2\sigma^2} + \frac{ip_\beta}{\hbar}(q - q_\beta)\right). \tag{A2}$$

Let the reference trajectory, labeled $\gamma$, connect $q_0$ to $q_t$ in a time $t$. There is a very slight generalization here relative to the exposition in [29] where the initial conditions of the reference trajectory are taken at $(q_\alpha, p_\alpha)$. The quadratically expanded action about $\gamma$, $S_\gamma(q, q'; t)$ is

$$S_\gamma(q, q'; t) = S(q_t, q_0; t) + \left(\frac{\partial S}{\partial q}\right)_{q_t}(q - q_t) + \left(\frac{\partial S}{\partial q'}\right)_{q_0}(q' - q_0) + \left(\frac{\partial^2 S}{\partial q^2}\right)_{q_t}\frac{(q - q_t)^2}{2}$$

$$+ \left(\frac{\partial^2 S}{\partial q'^2}\right)_{q_0}\frac{(q' - q_0)^2}{2} + \left(\frac{\partial^2 S}{\partial q \partial q'}\right)_{q_t, q_0}(q - q_t)(q' - q_0), \tag{A3}$$

where the first derivatives are, to within a sign, the final and initial momenta,

$$\left(\frac{\partial S}{\partial q}\right)_{q_t} = p_t, \qquad \left(\frac{\partial S}{\partial q'}\right)_{q_0} = -p_0. \tag{A4}$$

The linearized equations of motion are expressed with the stability matrix $M$. Initial deviations around a reference trajectory $\gamma$ are expressed as

$$\left(\begin{array}{c} \partial p_t \\ \partial q_t \end{array}\right) = M_\gamma \left(\begin{array}{c} \partial p_0 \\ \partial q_0 \end{array}\right), \qquad M_\gamma = \left(\begin{array}{cc} m_{11} & m_{12} \\ m_{21} & m_{22} \end{array}\right). \tag{A5}$$

The second derivatives can be expressed as combinations of the stability matrix elements giving

$$\left(\frac{\partial^2 S}{\partial q^2}\right)_{q_t} = \frac{m_{11}}{m_{21}}, \qquad \left(\frac{\partial^2 S}{\partial q'^2}\right)_{q_0} = \frac{m_{22}}{m_{21}}, \qquad \left(\frac{\partial^2 S}{\partial q \partial q'}\right)_{q_t, q_0} = \frac{-1}{m_{21}}. \tag{A6}$$

Then

$$C_{\beta\alpha}(t) = \left(\frac{1}{2\pi i \hbar |m_{21}|}\right)^{1/2} \int_{-\infty}^{\infty} dq \, dq' \, \phi_\beta^*(q)\phi_\alpha(q') \exp\left(iS_\gamma(q, q'; t)/\hbar - \frac{i\pi\nu}{2}\right) \tag{A7}$$

With

$$A_0 = m_{11} + m_{22} + i\left(\frac{\hbar m_{21}}{\sigma^2} - \frac{m_{12}\sigma^2}{\hbar}\right), \quad \delta q_\alpha = \frac{q_\alpha - q_0}{\sigma},$$

$$A_1 = m_{22} - i\frac{m_{12}\sigma^2}{\hbar}, \quad \delta q_\beta = \frac{q_\beta - q_t}{\sigma},$$

$$A_2 = m_{11} - i\frac{m_{12}\sigma^2}{\hbar}, \quad \delta p_\alpha = \frac{(p_\alpha - p_0)\sigma}{\hbar}, \tag{A8}$$

$$A_3 = m_{11} + i\frac{\hbar m_{21}}{\sigma^2}, \quad \delta p_\beta = \frac{(p_\beta - p_t)\sigma}{\hbar},$$

$$A_4 = m_{22} + i\frac{\hbar m_{21}}{\sigma^2}.$$

The final result is

$$C_{\beta\alpha}(t) = \left(\frac{2}{A_0}\right)^{1/2} \exp\left( \frac{i}{\hbar}[S_\gamma(q_t, q_0; t) + p_\beta(q_\beta - q_t) - p_\alpha(q_\alpha - q_0)] - \frac{i\pi\nu}{2} \right.$$

$$-\frac{1}{2A_0}[A_1\delta q_\alpha^2 + A_2\delta q_\beta^2 + A_3\delta p_\alpha^2 + A_4\delta p_\beta^2 - 2(\delta q_\alpha + i\delta p_\alpha)(\delta q_\beta - i\delta p_\beta)$$

$$\left. -2iA_3\delta q_\alpha\delta p_\alpha + 2iA_4\delta q_\beta\delta p_\beta] \right). \tag{A9}$$

## APPENDIX B: A FFT FOR THE SOFT WALLED QUANTUM STADIUM

We were interested in a direct time-dependent method of generating extremely accurate quantum propagation since the semiclassical results were so good. Preliminary attempts at a finite-difference method did not look extremely promising, although Christoffel and Brumer [21] have reported good results with a method of this kind. We turned to developing a standard fast Fourier transform, split-operator method (FFT) on a rectilinear grid.

The FFT successively applies the kinetic and potential propagation operators, respectively, for differential time steps. It is important that the potential unitary operator not skip (not vary) factors of $2\pi$ between neighboring grid points. Otherwise, the propagation is no longer faithful.

Therefore, the FFT cannot handle infinite walls. However, an extremely good soft-wall version can be easily written. Our first attempt at a stadium FFT incorporated a finite well depth, yet the potential still rose discontinuously. It was found not to converge well enough for our taste. A second attempt was to soften the wall with a Woods-Saxon cross-sectional shape. The stadium is then more accurately imagined as a bathtub-shaped well with very steep walls and a flat bottom. Using the potential (for the direction perpendicular to the wall)

$$V = \frac{V_0}{1 + a\exp[b(1 - q^2)]}, \tag{B1}$$

the FFT was found to converge properly and extremely accurately if (i) the wall was very steep but required at

least one grid spacing distance to rise from, say, the 10% to 90% level (this fixes the scale of $b$), (ii) the grid spacing was not more than about $\frac{1}{20}$th of a wavelength, (iii) the time step was taken so that the wave moved no more than about one grid spacing in one step, and (iv) the wall was not too high, yet high enough to be well above the maximum energy component of the initial state (thus fixing $V_0$ and $a$).

The convergence was demonstrated to be excellent by checks such as (i) calculating the energy expectation as a function of time, (ii) comparing differing grid sizes and steepness of walls, (iii) creating real-time movies to watch the waves propagate, and (iv) having the superb agreement with the semiclassical theory.

[1] V. P. Maslov and M. V. Fedoriuk, *Semiclassical Approximations in Quantum Mechanics* (Reidel, Dordrecht, 1981).

[2] M. C. Gutzwiller, J. Math. Phys. **12**, 343 (1971), and references therein.

[3] R. Balian and C. Bloch, Ann. Phys. (N.Y.) **69**, 76 (1972).

[4] S. Tomsovic and E. J. Heller, Phys. Rev. Lett. **67**, 664 (1991).

[5] M. Sieber and F. Steiner, Physica D **44**, 248 (1990); G. Tanner, P. Scherer, E. B. Bogomolny, B. Eckhardt, and D. Wintgen, Phys. Rev. Lett. **67**, 2410 (1991); P. Cvitanovic and B. Eckhardt, *ibid.* **63**, 823 (1989); M. V. Berry and J. P. Keating, J. Phys. A **23**, 4839 (1990).

[6] The focus issue on periodic orbit theory, Chaos **2** (1992).

[7] See *Chaos and Quantum Physics*, edited by M.J. Giannoni, A. Voros, and J. Zinn-Justin, Les Houches Session LII, 1989 (Elsevier, Amsterdam, 1991).

[8] R. V. Jensen, Nature **355**, 311 (1992).

[9] E. B. Bogomolny, Physica D **31**, 169 (1988).

[10] A. M. Ozorio de Almeida, Nonlinearity **2**, 519 (1989).

[11] A. Voros, J. Phys. A **21**, 685 (1988).

[12] J. H. Van Vleck, Proc. Natl. Acad. Sci. **14**, 178 (1928).

[13] M. C. Gutzwiller, J. Math. Phys. **8**, 1979 (1967).

[14] E. J. Heller, J. Chem. Phys. **94**, 2723 (1991).

[15] Patrick W. O'Connor, Steven Tomsovic, and Eric J. Heller, Physica D **55**, 340 (1992); Patrick W. O'Connor and Steven Tomsovic, Ann. Phys. (N.Y.) **207**, 218 (1991).

[16] M. Sepúlveda, S. Tomsovic, and E. J. Heller, Phys. Rev. Lett. **69**, 402 (1992).

[17] M. V. Berry and N. L. Balazs, J. Phys. A **12**, 625 (1979).

[18] M. V. Berry, N. L. Balazs, M. Tabor, and A. Voros, Ann. Phys. (N.Y.) **122**, 26 (1979).

[19] Z. V. Lewis, Ph.D. dissertation, University of Bristol, 1982; see also M. V. Berry, Ann. (N.Y.) Acad. Sci. **357**, 183 (1983).

[20] P. W. O'Connor, Ph.D. dissertation, University of Washington, 1991; P. W. O'Connor, S. Tomsovic, and E. J. Heller, J. Stat. Phys. **68**, 131 (1992).

[21] K. M. Christoffel and P. Brumer, Phys. Rev. A **33**, 1309 (1986).

[22] C. M. Marcus, A. J. Rimberg, R. M. Westervelt, P. F. Hopkins, and A. C. Gossard (unpublished).

[23] J. Stein and H.-J. Stöckman (unpublished); see also S. Sridhar and E. J. Heller, Phys. Rev. A **46**, R1728 (1992).

[24] E. Doron and U. Smilansky, Phys. Rev. Lett. **68**, 1255 (1992).

[25] R. P. Feynman and A. R. Hibbs, *Quantum Mechanics and Path Integrals* (McGraw-Hill, New York, 1965).

[26] L. S. Schulman, *Techniques and Applications of Path Integration* (Wiley, New York, 1981).

[27] D. Huber, E. J. Heller, and R. G. Littlejohn, J. Chem. Phys. **89**, 2003 (1988).

[28] E. J. Heller, J. Chem. Phys. **62**, 1544 (1975); R. G. Littlejohn, Phys. Rep. **138**, 193 (1986).

[29] E. J. Heller, in Ref. [7].

[30] E. J. Heller, Phys. Rev. Lett. **53**, 1515 (1984).

[31] Ya Sinai, Funct. Anal. Appl. **2**, 61 (1968); R. Bowen, Am. J. Math. **95**, 429 (1973).

[32] G. D. Birkhoff, Acta Math. **43**, 1 (1922).

[33] J. Moser, Commun. Pure Appl. Math. **9**, 673 (1956).

[34] S. Tomsovic and E. J. Heller (unpublished).

[35] G. M. Zaslovsky, Phy. Rep. **80**, 157 (1981).

[36] L. A. Bunimovich, Funct. Anal. Appl. **8**, 254 (1974); Commun. Math. Phys. **65**, 295 (1979).

[37] S. McDonald, Ph.D. dissertation, University of California, Berkeley, 1983.

[38] O. Bohigas, M.-J. Giannoni, and C. Schmit, J. Phys. (Paris) Lett. **45**, L-1015 (1984).

[39] R. Blümel, I. H. Davidson, W. P. Reinhardt, H. Lin, and M. Sharnoff, Phys. Rev. A **45**, 2641 (1992).

FIG. 1.   A schematic illustration of the hyperbolic structure of phase space. The swarm of trajectories, i.e., the black disk, exponentially stretches apart as time evolves from upper left to lower right.  The light gray disks indicate the initial swarm and the medium gray javelin shows the local linear-dynamical approximation.
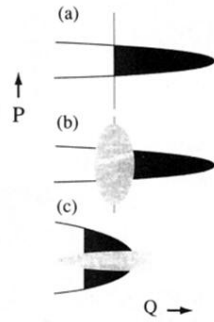
FIG. 4. The area-$\hbar$ rule. (a) The area contained between intersections of the time evolved manifold of a state and a position state (vertical line) is shown as black. If this area falls below $\hbar$, the semiclassical amplitude is in doubt. (b) A coherent state of the type shown is subject to nearly the same area rule. (c) If it is squeezed more like a momentum state, no caustic problems arise.